A comparison of magnetic field measurements and a plasma-based proxy to infer EMIC wave distributions at geosynchronous orbit

L. W. Blum,[1] E. A. MacDonald,[2] L. B. N. Clausen,[3,4] and X. Li[1]

Received 23 December 2011; revised 27 March 2012; accepted 28 March 2012; published 11 May 2012.

[1] Wave-particle interactions are fundamental to the dynamics of the outer radiation belt. Electromagnetic ion cyclotron (EMIC) waves can resonate with energetic electrons, causing pitch angle diffusion and scattering of the electrons into Earth's atmosphere. These waves act locally; thus, accurately measuring their spatial and temporal distributions is critical to understanding their contribution to radiation belt electron losses. Using Los Alamos National Laboratory Magnetospheric Plasma Analyzer data from geosynchronous orbit, we examine a plasma-based proxy for enhanced EMIC wave growth during a set of 52 relativistic electron flux dropout events. This proxy is compared to in situ wave measurements from the GOES satellites, also at geosynchronous orbit, for single-wave events as well as a superposed epoch statistical analysis. The proxy is extended to calculate an amplitude for the inferred waves, to enable a more quantitative comparison to the in situ GOES EMIC measurements. Signatures of EMIC waves are present in both the proxy and the direct wave observations at similar local times as well as epoch times. The waves are most prevalent in the afternoon sector, with enhanced occurrences beginning half a day before the onset of the dropouts and peaking in the day following. We see agreement in occurrence between the proxy and waves both statistically and in individual instances. This study demonstrates the powerful applications of plasma data to infer wave distributions in space.

Citation: Blum, L. W., E. A. MacDonald, L. B. N. Clausen, and X. Li (2012), A comparison of magnetic field measurements and a plasma-based proxy to infer EMIC wave distributions at geosynchronous orbit, *J. Geophys. Res.*, *117*, A05220, doi:10.1029/2011JA017474.

1. Introduction

[2] Wave-particle interactions play a critical role in radiation belt dynamics, and can provide a major source of both acceleration and loss of energetic electrons in the inner magnetosphere. In particular, electromagnetic ion cyclotron (EMIC) waves can gyroresonate with energetic electrons, breaking their first adiabatic invariant and scattering them into the loss cone [*Albert*, 2003; *Summers and Thorne*, 2003]. EMIC waves are generated in the inner magnetosphere by anisotropic ($T_\perp > T_\parallel$) keV ion populations as the ions convect in from the tail and drift westward around the Earth [e.g., *Anderson et al.*, 1996]. Large anisotropies, as well as the presence of cool plasma, can produce enhanced EMIC wave growth [*Cornwall et al.*, 1970; *Horne and Thorne*, 1993]. In order to better quantify losses to radiation belt electrons due to EMIC waves, an understanding of the waves' global distribution is needed. As these waves are a localized phenomenon, multipoint measurements are necessary to accurately measure EMIC distributions and determine the spatial and temporal extent of the waves.

[3] EMIC waves often occur in the afternoon sector where ring current ions overlap cool, dense plasmaspheric plumes [*Spasojević et al.*, 2004]. A number of studies have examined the distributions of EMIC waves across local time and L shell using magnetometer measurements from a variety of satellites including CRRES, GOES, AMPTE CCE, and DE 1 [e.g., *Meredith et al.*, 2003; *Clausen et al.*, 2011; *Anderson et al.*, 1992; *Erlandson and Ukhorskiy*, 2001]. The waves are observed primarily on the dusk side, with occurrences peaking during the main phase of storms but often persisting into the recovery phase as well [*Fraser and Nguyen*, 2001; *Bossen et al.*, 1976; *Halford et al.*, 2010]. While in situ EMIC measurements show strong wave activity during the main phase of storms, a relative absence is observed in ground measurements of Pc1–Pc2 waves during this storm phase [*Engebretson et al.*, 2008, *Posch et al.*, 2010]. Various indirect measures of the waves have also been used to gain insight into their global distributions. *Spasojevic and Fuselier* [2009] investigated the correspondence between

[1]Laboratory for Atmospheric and Space Physics, University of Colorado Boulder, Boulder, Colorado, USA.
[2]Los Alamos National Laboratory, Los Alamos, New Mexico, USA.
[3]Bradley Department of Electrical and Computer Engineering, Virginia Polytechnic Institute and State University, Blacksburg, Virginia, USA.
[4]Now at Institute for Geophysics and Extraterrestrial Physics, TU Braunschweig, Braunschweig, Germany.

Corresponding author: L. W. Blum, Laboratory for Atmospheric and Space Physics, University of Colorado Boulder, 1234 Innovation Dr., Boulder, CO 80303-7814, USA. (lauren.blum@colorado.edu)

Copyright 2012 by the American Geophysical Union.
0148-0227/12/2011JA017474

Table 1. Values for Constants σ and a in the Expressions for Fitting Parameters S_h (Equation (2a)) and α_h (Equation (2b)), Calculated for Three Different Local Temporal Growth Rates γ/Ω_p

γ/Ω_p	σ_0	σ_1	σ_2	a_0	a_1	a_2
0.001	0.429	0.124	0.0118	0.409	0.0145	0.00028
0.004	0.535	0.171	0.0224	0.403	0.0215	0.00111
0.01	0.664	0.249	0.0438	0.403	0.0289	0.00229

EMIC waves and proton precipitation in detached subauroral arcs as seen in far ultraviolet (FUV) images. *Spasojevic et al.* [2011] also find a correlation between these auroral arcs and the local plasma conditions in the equatorial plane that map to the regions of precipitation.

[4] In this study, we use in situ plasma measurements from the Los Alamos National Laboratory (LANL) instruments onboard geosynchronous satellites to calculate a plasma-based proxy for EMIC waves based on Alfvén cyclotron instability theory [*Gary et al.*, 1994; *Blum et al.*, 2009]. The proxy, detailed in *Blum et al.* [2009], is examined and compared to in situ wave measurements from the GOES satellites to investigate the accuracy and validity of such a proxy over local time during periods around relativistic electron drop out events. This proxy is extended to calculate wave amplitude to enable more quantitative comparison to the wave observations. We look both at single events, as well as the statistical distributions of the waves, and compare the LANL proxy to GOES EMIC wave measurements.

2. EMIC Wave Proxy

[5] Using the formulation described in *Blum et al.* [2009], similar to one used to investigate whistler chorus mode waves by *MacDonald et al.* [2008], a proxy for EMIC wave growth is calculated based on local plasma conditions. Theory and simulations establish that sufficiently anisotropic ions can trigger the Alfvén cyclotron instability and excite EMIC waves [*Gary*, 1993]. The incited fluctuations are resonant with and can scatter the source ions, reducing the anisotropy and quenching the instability. Thus an upper bound for stability is imposed on the ion anisotropy:

$$\frac{T_{\perp h}}{T_{||h}} - 1 = \frac{S_h}{\beta_{||h}^{\alpha_h}}, \tag{1}$$

where subscript h indicates the warm ion population; plasma beta $\beta_{||h} = 8\pi n_h T_{||h}/B_o^2$; n_h is the warm ion density; and $T_\perp$ and $T_\parallel$ are the ion temperatures perpendicular and parallel, respectively, to the background magnetic field B_o. S_h and α_h are parameters obtained by a fit to the instability threshold condition derived from linear theory. They are functions of γ/Ω_p as well as n_h/n_e, where γ is the temporal growth rate, Ω_p is the proton gyrofrequency, and n_e is the electron density, taken to be equal to the sum of the warm and cool ion populations [*Gary et al.*, 1994]. These fitting parameters are described by the following expressions [*Blum et al.*, 2009]:

$$S_h = \sigma_0 + \sigma_1 \ln(n_h/n_e) + \sigma_2[\ln(n_h/n_e)]^2 \tag{2a}$$

and

$$\alpha_h = a_0 + a_1 \ln(n_h/n_e) + a_2[\ln(n_h/n_e)]^2. \tag{2b}$$

Table 1 provides the values of the constants σ and a calculated for various growth rates.

[6] *Blum et al.* [2009] define an observational EMIC parameter:

$$\Sigma_h = \left(\frac{T_{\perp h}}{T_{||h}} - 1\right)\beta_{||h}^{\alpha_h}. \tag{3}$$

As α_h is a very weak function of γ/Ω_p, we use the expression for α_h associated with $\gamma/\Omega_p = 10^{-3}$ in all calculations of Σ_h. For $\Sigma_h > S_h$ at a given time, it is likely that the warm ions are sufficiently anisotropic to excite the Alfvén cyclotron instability and generate waves at the prescribed growth rate. Thus, comparing the two quantities Σ_h and S_h yields a proxy for determining the level of enhanced EMIC wave activity. Where $\Sigma_h = S_h$ for a given temporal growth rate γ, wave growth of this rate is expected.

[7] In this work, this proxy is further developed to calculate physical wave characteristics and enable a more quantitative comparison to direct wave measurements. Using S_h expressions for γ/Ω_p = 0.001, 0.004, and 0.01, and interpolating linearly between these values, a γ value is found for each Σ_h measurement such that $\Sigma_h = S_h(\gamma/\Omega_p)$. Next, using the warm plasma dispersion relation and following *Kozyra et al.* [1984, equation 4], the group velocity is calculated, and thus the convective growth rate (γ/v_g) for the waves. Following *Jordanova et al.* [1997] and *Chen et al.* [2010], the path-integrated gain G is calculated in decibels by integrating the convective growth rate along the source region of the field line:

$$G = 20\log_{10} e^{\int_{\lambda_1}^{\lambda_2} \gamma/v_g \, ds}, \tag{4}$$

where λ_1 and λ_2 are the lower and upper limits of the source region. We assume parallel propagating waves, a dipole magnetic field, the source region to be $\pm$ 10° magnetic latitude, and the growth rate and group velocity to be constant within this region.

[8] Finally, we adopt the simple scaling model used by *Jordanova et al.* [2001] to compute a wave amplitude B_w:

$$B_w = B_{sat} \times 10^{(G - G_{\max})/G_{\min}}, \tag{5}$$

where B_{sat} is the saturation amplitude of the waves; G_{max} is a maximum gain, above which saturation is assumed; and G_{min} the minimum gain, below which growth and wave-particle scattering is considered to be negligible. Comparing to statistical studies of EMIC wave amplitudes, which typically measure waves to be ~1–3 nT in the inner magnetosphere, with a maximum observed magnitude ~10 nT [*Erlandson and Ukhorskiy*, 2001; *Anderson et al.*, 1992], we set B_{sat} = 10 nT, G_{min} = 13.3 (equivalent to an amplitude of 0.1 nT), and G_{max} = 40 (10 nT). Below this G_{min} value, waves drop below magnitudes detectable by the GOES spacecraft. To better match wave amplitudes measured by GOES, our selections for these values differ from those used by *Jordanova et al.*, [2001], who takes G_{min} = 20 and G_{max} = 60. While this amplitude calculation includes a number of assumptions, it allows for estimation of physical wave characteristics, for quantitative comparison to the wave measurements themselves.

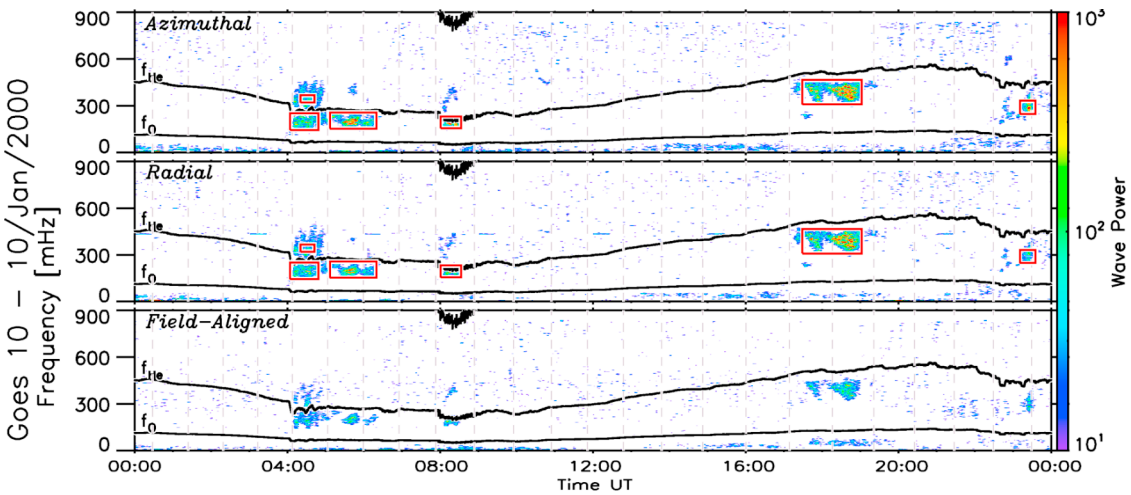

Figure 1. Spectrograms of GOES 0.512 s magnetometer data. Wave powers are shown in the azimuthal, radial, and field-aligned directions, with respect to the background magnetic field. Red boxes indicate activity identified as EMIC waves, as selected by the *Clausen et al.* [2011] algorithm.

We discuss the implications of these assumptions in more detail in section 4.

3. Observations

[9] LANL data from geosynchronous orbit are used to investigate the in situ plasma conditions during our events. Using the Magnetospheric Plasma Analyzer (MPA) instrument, bulk moments are obtained for the density of cool ions (defined as <100 eV), the density of warm ions (100 eV to 45 keV), as well as the warm ion temperature both parallel and perpendicular to the background magnetic field ($T_{\parallel}$ and $T_{\perp}$, respectively). As MPA cannot distinguish among ion species, a pure proton population is assumed. The background magnetic field direction is inferred from symmetry in the plasma distributions [*Thomsen et al.*, 1999]. The T89 magnetic field model [*Tsyganenko*, 1989] is used to calculate the magnitude of the background field B_o.

[10] The inferred waves are compared to wave measurements taken by the GOES satellites, also at geosynchronous orbit. Using 0.512 s high-resolution magnetometer data, resampled at a constant resolution of 0.6 s, dynamic spectra are computed for all three magnetic field components using a fast Fourier transform (FFT) with a 1 h window, advanced in 20 min steps, following the analysis performed by *Clausen et al.* [2011]. The instrument response is suppressed for frequencies between 0.5 and 1.0 Hz, so only EMIC waves with amplitudes >1 nT are resolvable up to ~0.8 Hz, and amplitudes >0.1 nT below 0.5 Hz [*Fraser et al.*, 2010]. This enables identification of waves in the He^+ and O^+ bands, and the lower portion of the H^+ band. To automate identification of EMIC waves from the spectrograms, an algorithm developed and described by *Clausen et al.* [2011] is employed. This algorithm selects waves between 0.1 and 0.8 Hz, with total power spectral density in the transverse components greater than 10 nT^2/Hz above the background noise lasting 15 min or more. Figure 1 demonstrates the output of this algorithm for a single day of GOES data, where the red boxes indicate EMIC wave selections.

[11] Using these data sets, we perform both single event comparisons as well as a superposed epoch study of 52 events. For the statistical study, a set of energetic electron flux dropouts taken from *Green et al.* [2004] is used, where events were chosen based on a decrease in the >2 MeV electron flux, as measured by GOES, by a factor of 100 or greater when compared to the flux on the previous day. On average, these events show a dip in Dst reaching a minimum of −40 nT in the day following dropout onset (zero epoch). While *Green et al.* [2004] looked at these events to investigate the potential causes of the relativistic electron dropouts, they are used here as a convenient event list for which both LANL and high-resolution GOES data are available. Investigation of the link between the waves and the radiation belt depletions is not the focus of the present study. Below, we first present GOES and LANL data from a single day during one such dropout event, and then place it in the larger context of the statistical study.

3.1. Single-Event Study: 10 January 2000

[12] Data are presented from the GOES 10 and LANL-89 (1989–046) satellites for one such event on 10 January 2000, where LANL-89 trails GOES by 2 h. This dropout event, with zero epoch occurring at 5 UT, takes place just prior to the onset of a geomagnetic storm, with minimum Dst reaching −81 nT on 11 January around 22 UT. This day is selected for comparison because GOES detects EMIC waves at 5 distinct times throughout the day; we investigate the accuracy of the plasma-based proxy for each of these instances of wave activity, which are distributed across a range of local times. On 10 January, EMIC waves are measured first by GOES at 4 UT, followed by subsequent bursts at roughly 5, 8, 17:30, and 23:10 UT (see Figure 1).

[13] The various plasma parameters measured by LANL MPA and used to calculate the EMIC proxy are presented in Figure 2. Figure 2a shows the cold plasma density, enhancements indicating crossings into plasmaspheric bulge or plume regions. Figure 2b shows warm proton density, and Figure 2c the warm proton temperature anisotropy,

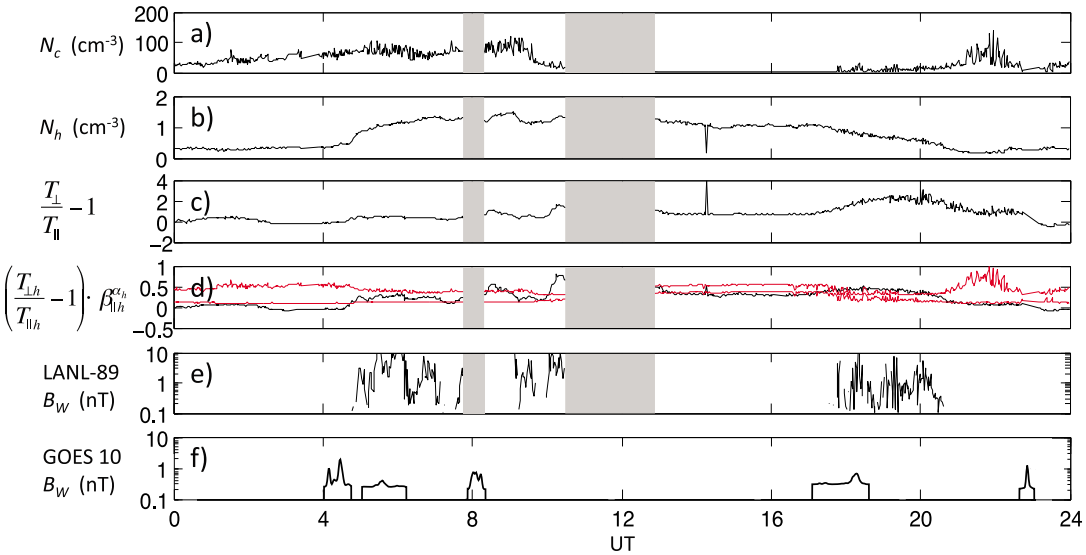

Figure 2. LANL-89 MPA data for 10 January 2000. (a) Cool proton density, (b) warm proton density, and (c) warm proton anisotropy are shown versus universal time (UT). (d) The EMIC wave proxy Σ_h in black, calculated following equation (3). We have included calculations of the theoretical instability threshold S_h for local growth rates of 10^{-3} (lower red line) and 10^{-2} (upper red line), following equation (2a) and using values found in Table 1. The instability threshold for a growth rate of $\gamma/\Omega_p = 10^{-3}$ is exceeded at four different instances. Grey-shaded regions are periods where MPA data are unavailable. (e) The calculated wave amplitude during the four times when the threshold is exceeded. (f) The EMIC wave amplitudes measured by GOES 10 are presented for comparison.

defined as $T_\perp/T_\parallel - 1$. Elevated anisotropies, concurrent with enhanced cool and warm plasma densities, combine to create four separate times where the proxy exceeds the instability threshold for a growth rate $\gamma/\Omega_p = 10^{-3}$ (Figure 2d). For these times, the wave amplitude is calculated (Figure 2e) following the steps previously outlined in section 2. In Figure 2f, average amplitudes of the EMIC waves measured by GOES 10 are shown. GOES amplitudes are approximated by calculating the square root of the wave power, integrated over the frequency range of the activity as identified by the *Clausen et al.* [2011] algorithm described in section 3. When waves in multiple bands are detected simultaneously (e.g., 4–5 UT), the average amplitude of the two wave bursts is calculated, as the LANL EMIC proxy does not distinguish the exact frequency of the EMIC activity it infers. Simultaneous waves in multiple bands are measured relatively infrequently (during roughly 2% of the GOES wave detections) so we do not expect this to greatly affect our statistical results. From Figures 2e and 2f, it is evident that each EMIC wave burst measured by GOES 10 is subsequently detected in the LANL-89 data.

3.2. Statistical Superposed Epoch Study

[14] The LANL spacecraft are not equipped with field measurements, and GOES 8, 9, and 10 do not provide the necessary plasma parameters to calculate the EMIC proxy. Thus, the conclusions drawn from single event comparisons of wave amplitude are limited by the physical separation of the spacecraft. Therefore, we perform a superposed epoch study of 52 relativistic electron flux dropout events and compare EMIC wave distributions across both local and epoch times. Following *Green et al.* [2004], events are superposed to align the onsets of the electron dropouts, where zero epoch is set to the time when the >2 MeV electron flux drops by a factor of two as compared to the flux level on the previous day. On average, minimum Dst falls within 1 day after zero epoch and a small SSC (storm sudden commencement) is observed just before zero epoch, so for events associated with storms, the dropouts occur primarily during the main phase [*Green et al.*, 2004, Figure 5]. There is also, on average, an increase in AE activity coinciding with zero epoch. These events are often preceded by increased solar wind dynamic pressure and a southward turning of the interplanetary magnetic field [*Green et al.*, 2004].

[15] Figure 3 shows normalized occurrence rates of both the plasma-based LANL proxy (Figure 3a), as well as the GOES EMIC wave measurements (Figure 3b). The LANL data set utilizes measurements from 6 spacecraft distributed in local time, while GOES includes data from the GOES 8, 9, and 10 spacecraft depending on availability. For each data set, the number of measurements made during EMIC activity (measured or inferred), divided by the total number of measurements in that time bin, is plotted. Data are divided into hourly bins, and average values within each bin are plotted; gray bins indicate times with no data. We choose a minimum amplitude of 0.1 nT for the lower threshold of the LANL proxy, to best match the GOES instrument sensitivity. Here, the proxy and wave measurements agree well qualitatively across both local and epoch time. The majority of EMIC waves, ~65% of those measured by GOES and 69% inferred by LANL, occur between 12 and 18 MLT, in agreement with

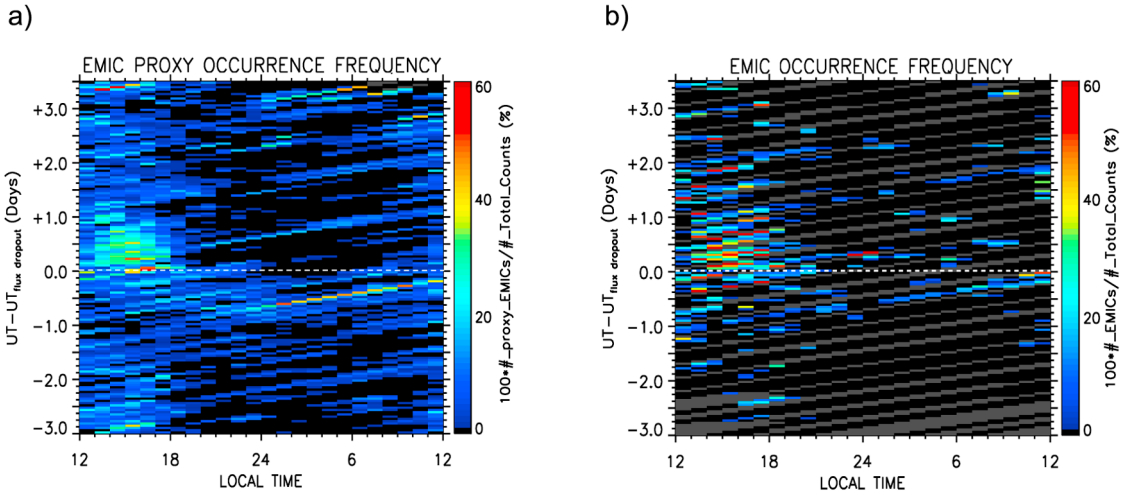

Figure 3. Distributions of EMIC wave occurrences over local and epoch times from (a) the plasma-based proxy from LANL MPA data and (b) wave measurements from GOES. The color bar indicates normalized occurrence rates of the waves in hourly time bins.

other EMIC measurements seen by CRRES [*Meredith et al.*, 2003] and GOES [*Clausen et al.*, 2011].

4. Discussion

4.1. Wave Occurrence Comparison

[16] We return to the case study previously presented to validate the proxy for individual events, with the caveat that wave characteristics may be varying in the 2 h of local time between GOES 10 and LANL-89. Figure 2 shows the plasma conditions combining to exceed the local instability threshold and incite EMIC wave activity at 4 times throughout the day, each slightly later in universal time than the wave activity detected by GOES 10. The first two periods of wave activity detected by LANL (just after 4 UT through ~9:30 UT) occur during periods of enhanced cold plasma as the satellite passes through the dusk sector. In contrast, the fourth occurrence of EMIC activity, beginning at LANL-89 around 17:30 UT, occurs on the morning side, where cold plasma density remains low but warm ion anisotropy is enhanced. At ~21 UT, as cold plasma density increases again, the warm plasma density drops to very low values, elevating the instability threshold (Figure 2d) and making wave growth more difficult. Both cold plasma enhancements, as well as a large enough source population of warm ions, are needed to exceed the instability threshold and incite EMIC waves. We see the EMIC instability excited under various plasma conditions across a range of local times, in good agreement with observed EMIC waves. This case study demonstrates the validity of the plasma-based proxy across local times, and for a variety of plasma parameters that combine to trigger the instability.

[17] Figure 4 compares the statistical occurrence rates of the plasma-based proxy and EMIC wave measurements as a function of local and epoch time by averaging the occurrence frequencies from Figure 3 across epoch (Figure 4a) as well as a range of local times (Figures 4b–4e). Figure 4a shows the distribution of LANL and GOES measurements across local time, and demonstrates the coherence between the proxy and wave occurrences over local time. There is a strong peak in both LANL and GOES from ~12 to 18 MLT, with a linear correlation coefficient of 0.96 between the two, and a mean difference over all local times of 1.37%. At local times beyond this peak, somewhat larger wave occurrences exist in the LANL proxy than in GOES. These slightly elevated LANL values are also revealed when comparing across epoch time for various MLTs (see Figures 4b–4e). This suggests that the plasma instability may be triggered without exciting EMIC waves of large enough amplitude for detection by GOES.

[18] We focus on Figure 4b, which averages EMIC occurrences from 12 through 17 MLT, as this is the region in which the majority of the waves occur. Occurrence rates are elevated in both the LANL proxy and the GOES data beginning half a day before the onset of the dropouts and extending 1 day following, with a peak just after zero epoch. Peak occurrence rates reach 20–30%, with a linear correlation coefficient of 0.81 and mean difference of 3.7% between the LANL proxy and GOES data. For events in this data set associated with storms, this occurrence peak falls in the main phase of the storms, consistent with other in situ measurements of EMIC waves but not necessarily with those from the ground [*Halford et al.*, 2010; *Engebretson et al.*, 2008]. As is evident from Figures 3 and 4, the greater coverage of the LANL satellites, both over time and longitude, provides an excellent database to draw from for statistical EMIC wave studies. Using the extensive LANL MPA database, it is possible to supplement current wave measurements and form a global picture of EMIC wave distributions at geosynchronous orbit during a variety of geomagnetic conditions.

4.2. Wave Amplitude Comparison

[19] Next we discuss the wave amplitude calculation, outlined in section 2, and compare the resulting inferred wave amplitudes to those measured by GOES. As mentioned in section 2, we use a source region of ± 10° magnetic latitude, as was used by *Jordanova et al.* [1997]. This is consistent with EMIC measurements from the CRRES satellite which indicate a source region constrained within ~± 11° magnetic latitude [*Loto'aniu et al.*, 2005]. However, the proxy wave

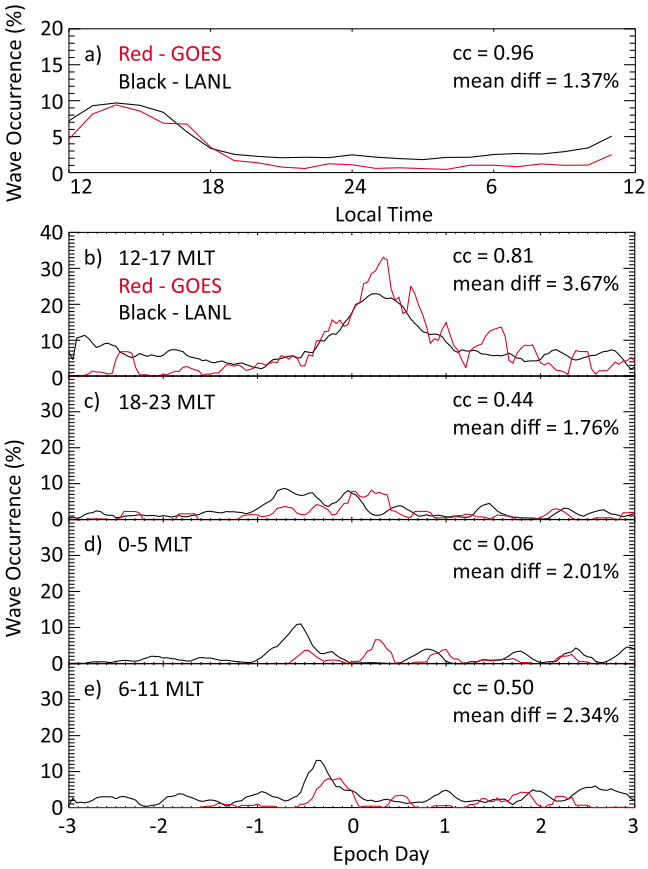

Figure 4. Smoothed occurrence frequencies of GOES EMIC wave measurements (red) and the LANL EMIC proxy (black) versus (a) local time and (b–e) epoch time. Figure 4a shows the distribution of waves over local time, averaged across all epoch days. Figures 4b–4e average occurrence rates across four local time sectors to show variation over epoch time. The measurements show agreement in both overall shape and magnitude. Mean differences as well as linear correlation coefficients between LANL and GOES occurrence rates are calculated for each panel.

amplitude calculation is fairly sensitive to this assumption (a region of $\pm$ 5° produces a wave gain roughly half as large as that for $\pm$ 10°), so while our source region choice is accurate statistically, it may be a source of uncertainty in gain, and thus wave magnitude, calculations for individual wave events.

[20] Additionally, we scale G_{min} = 13.3 to a wave amplitude of 0.1 nT, rather than the G_{min} = 20 used by *Jordanova et al.* [2001]. When using G_{min} = 20, there were far lower occurrence rates in the LANL data than the GOES, indicating that events with G < 20 were still able to incite EMIC wave growth. The G_{min} and G_{max} values used here are tuned to identify these smaller amplitude waves, and agree well with observations as well as theoretical calculations by *Bortnik et al.* [2011] for waves in the few nT range. However, the sensitivity of the scaling model (equation (5)) to larger gain values causes small increases in gain to result in large amplitude enhancements, potentially overestimating wave amplitudes at the upper end of the gain scale. As seen from the LANL amplitudes calculated for 10 January in Figure 2e, the proxy saturates on a number of occasions while the GOES measurements remain below ~2 nT. Measurements of >10 nT EMIC waves appear relatively rarely in the GOES data. We choose to use these lower G_{min} and G_{max} values of 13.3 and 40, respectively, in order to calculate accurate occurrence rates, despite the likely larger-than-realistic amplification of values at the upper end of the measurements.

[21] Figure 5 compares average wave amplitudes, measured and inferred, across both local and epoch time. As was done in Figure 4, the mean wave amplitudes in each hourly bin are now averaged across epoch time (Figure 5a) and local time (Figure 5b) to enable quantitative comparison of the LANL predicted amplitudes to those measured by GOES. Only bins where waves are detected are taken into consideration, so the GOES data are sparser, as seen in Figure 5b. The GOES data here also show more scatter around the mean, most likely due to fewer data points from the two GOES satellites when compared to all six of the LANL. As GOES wave occurrence rates are 0% for a number of hourly bins across the night and morning side, Figure 5b is not subdivided into four local time sectors, as was done for Figures 4b–4e. No obvious trends in variation in average amplitude are exhibited in relation to either epoch or local time, and the average magnitudes of the GOES and LANL measurements are very similar. The total distribution of wave amplitudes is also computed for all GOES wave detections as well as LANL proxy calculations, and distribution properties are compared. The mean amplitude measured by GOES across all local and epoch times is 1.12 nT, with a standard deviation of 0.43 nT, while the mean amplitude of waves inferred by LANL equals 1.13 nT, with a standard deviation of 1.6 nT. The average values agree well, as is also seen in Figure 5. The larger standard deviation in the LANL inferred wave amplitudes may be due to a greater sensitivity of the

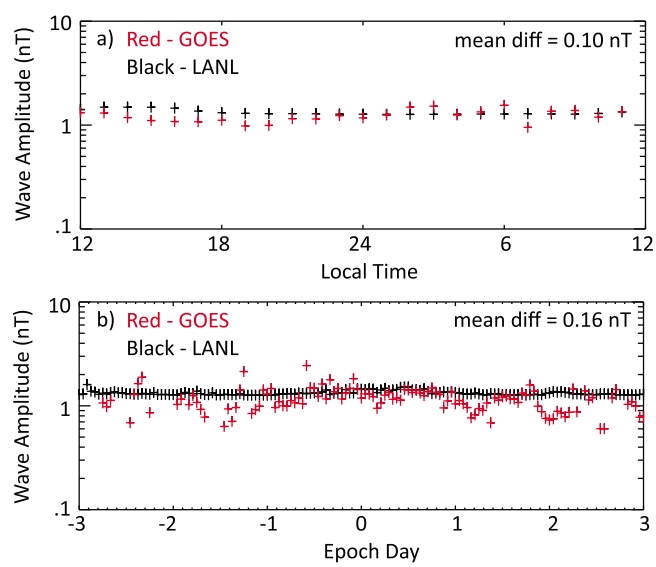

Figure 5. Average wave amplitudes measured by GOES (red) and calculated from the LANL EMIC proxy (black) across local and epoch time. No significant trends in amplitude variation as functions of either variable are observed. Average amplitudes calculated from LANL agree well with those measured by GOES.

proxy to low-amplitude waves as compared to the GOES instrument response, as well as to potential amplitude overestimation for events at the upper end of the gain range, as discussed earlier.

5. Conclusions

[22] In this study, direct EMIC wave measurements from the GOES satellites are compared to a plasma-based proxy for the waves, derived from warm (keV) ion temperature anisotropy and warm and cool ion population densities as measured by LANL satellites. We investigate the correlation between the plasma-based proxy and wave measurements at geosynchronous orbit both for individual cases as well as statistically across local and epoch times. Statistical EMIC occurrence rates from LANL and GOES both become elevated half a day before the onset of flux dropouts, peaking during the day following, and in the afternoon sector, consistent with theory and past observations. On 10 January 2000, as LANL-89 trailed GOES 10 by 2 h, EMIC wave signatures were detected in the plasma measurements at roughly the same local times as those measured by GOES magnetometers just previously. Each wave burst measured by GOES 10 is subsequently detected in the plasma conditions at LANL-89. Strong agreement is found between the wave and proxy occurrences both statistically as well as for single events.

[23] The ability to include LANL MPA data to complement wave measurements greatly enhances our understanding of EMIC wave distributions across local and storm times. As the LANL database consists of seven spacecraft spanning approximately 18 years, it contributes a vast number of measurements to supplement current EMIC wave statistics at geosynchronous orbit. This proxy validation also enables the use of LANL satellites to provide multipoint measurements of equatorial wave distributions, to compare both with other nearby satellites as well as to ground based wave measurements [e.g., *Posch et al.*, 2010] or low-altitude precipitation signatures [e.g., *Miyoshi et al.*, 2008; *Millan et al.*, 2010]. As seen from the EMIC activity on 10 January 2000 in Figure 2, this proxy could be used in combination with wave measurements to study the temporal and spatial variation for individual EMIC events. Additionally, as shown by *MacDonald et al.* [2010], this EMIC proxy combined with a similar proxy for whistler chorus waves can be used to study the relative contributions of various wave types to overall radiation belt dynamics through a balance of acceleration and scattering mechanisms. With the extension of the proxy to calculate EMIC wave amplitudes, an estimation of wave-particle scattering rates can be made, to aid in the quantification of relativistic electron losses from the outer radiation belt [*Bortnik et al.*, 2011]. Here, we demonstrate the value of plasma measurements to aid in the characterization of global EMIC wave distributions.

[24] **Acknowledgments.** The authors would like to acknowledge Janet Green at the NOAA Space Weather Prediction Center for providing the high-resolution GOES magnetometer data. The work at University of Colorado Boulder was supported by NSF 205 ATM-0842388. The Los Alamos portion of this work was supported by the Radiation Belt Storm Probes Energetic particle, Composition, and Thermal plasma science investigation under NASA contract award 923497 and was performed under the auspices of the U.S. Department of Energy (DOE). L. B. N. Clausen acknowledges funding from the NSF under grant ATM-0924919 and from the German Bundesministerium für Bildung und Forschung and the Deutsches Zentrum für Luft und Raumfahrt under contract 50OC0103.

[25] Robert Lysak thanks the reviewers for their assistance in evaluating this paper.

References

Albert, J. M. (2003), Evaluation of quasi-linear diffusion coefficients for EMIC waves in multispecies plasma, *J. Geophys. Res.*, *108*(A6), 1249, doi:10.1029/2002JA009792.

Anderson, B. J., R. E. Erlandson, and L. J. Zanetti (1992), A statistical study of Pc1–2 magnetic pulsations in the equatorial magnetosphere: 1. Equatorial occurrence distributions, *J. Geophys. Res.*, *97*(A3), 3075–3088, doi:10.1029/91JA02706.

Anderson, B. J., R. E. Denton, G. Ho, D. C. Hamilton, S. A. Fuselier, and R. J. Strangeway (1996), Observational test of local proton cyclotron instability in the Earth's magnetosphere, *J. Geophys. Res.*, *101*(A10), 21,527–21,543, doi:10.1029/96JA01251.

Blum, L. W., E. A. MacDonald, S. P. Gary, M. F. Thomsen, and H. E. Spence (2009), Ion observations from geosynchronous orbit as a proxy for ion cyclotron wave growth during storm times, *J. Geophys. Res.*, *114*, A10214, doi:10.1029/2009JA014396.

Bortnik, J., N. Omidi, L. Chen, R. M. Thorne, and R. B. Horne (2011), Saturation characteristics of electromagnetic ion cyclotron waves, *J. Geophys. Res.*, *116*, A09219, doi:10.1029/2011JA016638.

Bossen, M., R. L. McPherron, and C. T. Russell (1976), A statistical study of Pc1 magnetic pulsations at synchronous orbit, *J. Geophys. Res.*, *81*(34), 6083–6091, doi:10.1029/JA081i034p06083.

Chen, L., R. M. Thorne, V. K. Jordanova, C.-P. Wang, M. Gkioulidou, L. Lyons, and R. B. Horne (2010), Global simulation of EMIC wave excitation during the 21 April 2001 storm from coupled RCM-RAM-HOTRAY modeling, *J. Geophys. Res.*, *115*, A07209, doi:10.1029/2009JA015075.

Clausen, L. B. N., J. B. H. Baker, J. M. Ruohoniemi, and H. J. Singer (2011), EMIC waves observed at geosynchronous orbit during solar minimum: Statistics and excitation, *J. Geophys. Res.*, *116*, A10205, doi:10.1029/2011JA016823.

Cornwall, J. M., F. V. Coroniti, and R. M. Thorne (1970), Turbulent loss of ring current protons, *J. Geophys. Res.*, *75*(25), 4699–4709, doi:10.1029/JA075i025p04699.

Engebretson, M. J., et al. (2008), Pc1–Pc2 waves and energetic particle precipitation during and after magnetic storms: Superposed epoch analysis and case studies, *J. Geophys. Res.*, *113*, A01211, doi:10.1029/2007JA012362.

Erlandson, R. E., and A. E. Ukhorskiy (2001), Observations of electromagnetic ion cyclotron waves during geomagnetic storms: Wave occurrence and pitch angle scattering, *J. Geophys. Res.*, *106*(A3), 3883–3895, doi:10.1029/2000JA000083.

Fraser, B. J., and T. S. Nguyen (2001), Is the plasmapause a preferred source region of electromagnetic ion cyclotron waves in the magnetosphere?, *J. Atmos. Sol. Terr. Phys.*, *63*, 1225–1247, doi:10.1016/S1364-6826(00)00225-X.

Fraser, B. J., R. S. Grew, S. K. Morley, J. C. Green, H. J. Singer, T. M. Loto'aniu, and M. F. Thomsen (2010), Storm time observations of electromagnetic ion cyclotron waves at geosynchronous orbit: GOES results, *J. Geophys. Res.*, *115*, A05208, doi:10.1029/2009JA014516.

Gary, S. P. (1993), *Theory of Space Plasma Microinstabilities*, Cambridge Univ. Press, New York, doi:10.1017/CBO9780511551512.

Gary, S. P., M. B. Moldwin, M. F. Thomsen, D. Winske, and D. J. McComas (1994), Hot proton anisotropies and cool proton temperatures in the outer magnetosphere, *J. Geophys. Res.*, *99*, 23,603–23,615, doi:10.1029/94JA02069.

Green, J. C., T. G. Onsager, T. P. O'Brien, and D. N. Baker (2004), Testing loss mechanisms capable of rapidly depleting relativistic electron flux in the Earth's outer radiation belt, *J. Geophys. Res.*, *109*, A12211, doi:10.1029/2004JA010579.

Halford, A. J., B. J. Fraser, and S. K. Morley (2010), EMIC wave activity during geomagnetic storm and nonstorm periods: CRRES results, *J. Geophys. Res.*, *115*, A12248, doi:10.1029/2010JA015716.

Horne, R. B., and R. M. Thorne (1993), On the preferred source location for the convective amplification of ion cyclotron waves, *J. Geophys. Res.*, *98*(A6), 9233–9247, doi:10.1029/92JA02972.

Jordanova, V. K., J. U. Kozyra, A. F. Nagy, and G. V. Khazanov (1997), Kinetic model of the ring current-atmosphere interactions, *J. Geophys. Res.*, *102*(A7), 14,279–14,291, doi:10.1029/96JA03699.

Jordanova, V. K., C. J. Farrugia, R. M. Thorne, G. V. Khazanov, G. D. Reeves, and M. F. Thomsen (2001), Modeling ring current proton precipitation by electromagnetic ion cyclotron waves during the 14–16 May 1997 storm, *J. Geophys. Res.*, *106*(A1), 7–22, doi:10.1029/2000JA002008.

Kozyra, J. U., T. E. Cravens, A. F. Nagy, E. G. Fontheim, and R. S. B. Ong (1984), Effects of energetic heavy ions on electromagnetic ion cyclotron wave generation in the plasmapause region, *J. Geophys. Res.*, *89*(A4), 2217–2233, doi:10.1029/JA089iA04p02217.

Loto'aniu, T. M., B. J. Fraser, and C. L. Waters (2005), Propagation of electromagnetic ion cyclotron wave energy in the magnetosphere, *J. Geophys. Res.*, *110*, A07214, doi:10.1029/2004JA010816.

MacDonald, E. A., M. H. Denton, M. F. Thomsen, and S. P. Gary (2008), Superposed epoch analysis of a whistler instability criterion at geosynchronous orbit during geomagnetic storms, *J. Atmos. Sol. Terr. Phys.*, *70*, 1789–1796, doi:10.1016/j.jastp.2008.03.021.

MacDonald, E. A., L. W. Blum, S. P. Gary, M. F. Thomsen, and M. H. Denton (2010), High-speed stream driven inferences of global wave distributions at geosynchronous orbit: Relevance to radiation-belt dynamics, *Proc. R. Soc. A*, *466*, 3351–3362, doi:10.1098/rspa.2010.0076.

Meredith, N. P., R. M. Thorne, R. B. Horne, D. Summers, B. J. Fraser, and R. R. Anderson (2003), Statistical analysis of relativistic electron energies for cyclotron resonance with EMIC waves observed on CRRES, *J. Geophys. Res.*, *108*(A6), 1250, doi:10.1029/2002JA009700.

Millan, R. M., K. B. Yando, J. C. Green, and A. Y. Ukhorskiy (2010), Spatial distribution of relativistic electron precipitation during a radiation belt depletion event, *Geophys. Res. Lett.*, *37*, L20103, doi:10.1029/2010GL044919.

Miyoshi, Y., K. Sakaguchi, K. Shiokawa, D. Evans, J. Albert, M. Connors, and V. Jordanova (2008), Precipitation of radiation belt electrons by EMIC waves, observed from ground and space, *Geophys. Res. Lett.*, *35*, L23101, doi:10.1029/2008GL035727.

Posch, J. L., M. J. Engebretson, M. T. Murphy, M. H. Denton, M. R. Lessard, and R. B. Horne (2010), Probing the relationship between electromagnetic ion cyclotron waves and plasmaspheric plumes near geosynchronous orbit, *J. Geophys. Res.*, *115*, A11205, doi:10.1029/2010JA015446.

Spasojevic, M., and S. A. Fuselier (2009), Temporal evolution of proton precipitation associated with the plasmaspheric plume, *J. Geophys. Res.*, *114*, A12201, doi:10.1029/2009JA014530.

Spasojević, M., H. U. Frey, M. F. Thomsen, S. A. Fuselier, S. P. Gary, B. R. Sandel, and U. S. Inan (2004), The link between a detached subauroral proton arc and a plasmaspheric plume, *Geophys. Res. Lett.*, *31*, L04803, doi:10.1029/2003GL018389.

Spasojevic, M., L. W. Blum, E. A. MacDonald, S. A. Fuselier, and D. I. Golden (2011), Correspondence between a plasma-based EMIC wave proxy and subauroral proton precipitation, *Geophys. Res. Lett.*, *38*, L23102, doi:10.1029/2011GL049735.

Summers, D., and R. M. Thorne (2003), Relativistic electron pitch angle scattering by electromagnetic ion cyclotron waves during geomagnetic storms, *J. Geophys. Res.*, *108*(A4), 1143, doi:10.1029/2002JA009489.

Thomsen, M. F., E. Noveroske, J. E. Borovsky, and D. J. McComas (1999), Calculation of moments from measurements by the Los Alamos Magnetospheric Plasma Analyzer, *Rep. LA-13566-MS*, Los Alamos Natl. Lab., Los Alamos, N. M.

Tsyganenko, N. A. (1989), A magnetospheric magnetic field model with a warped tail current sheet, *Planet. Space Sci.*, *37*, 5–20, doi:10.1016/0032-0633(89)90066-4.